

Rydberg Excitons and Trions in Monolayer MoTe₂

Souvik Biswas, Aurélie Champagne, Jonah B. Haber, Supavit Pokawanvit, Joeson Wong, Hamidreza Akbari, Sergiy Krylyuk, Kenji Watanabe, Takashi Taniguchi, Albert V. Davydov, Zakaria Y. Al Balushi, Diana Y. Qiu, Felipe H. da Jornada, Jeffrey B. Neaton, Harry A. Atwater

ABSTRACT: Monolayer transition metal dichalcogenide (TMDC) semiconductors exhibit strong excitonic optical resonances, which serve as a microscopic, noninvasive probe into their fundamental properties. Like the hydrogen atom, such excitons can exhibit an entire Rydberg series of resonances. Excitons have been extensively studied in most TMDCs (MoS₂, MoSe₂, WS₂, and WSe₂), but detailed exploration of excitonic phenomena has been lacking in the important TMDC material molybdenum ditelluride (MoTe₂). Here, we report an experimental investigation of excitonic luminescence properties of monolayer MoTe₂ to understand the excitonic Rydberg series, up to 3s. We report a significant modification of emission energies with temperature (4 to 300 K), thereby quantifying the exciton-phonon coupling. Furthermore, we observe a strongly gate-tunable exciton-trion interplay for all the Rydberg states governed mainly by free-carrier screening, Pauli blocking, and band gap renormalization in agreement with the results of first-principles GW plus Bethe-Salpeter equation approach calculations. Our results help bring monolayer MoTe₂ closer to its potential applications in near-infrared optoelectronics and photonic devices.

KEYWORDS: Rydberg excitons, molybdenum ditelluride, exciton–electron interactions, optoelectronics, Rydberg trions, van der Waals semiconductor, near-infrared

Introduction

Excitons¹, excitations which consist of bound electron-hole pairs, in transition-metal dichalcogenide (TMDC) semiconductors are a suitable platform to investigate a rich variety of condensed-matter phenomena – such as Mott insulators^{2,3}, Wigner crystals⁴, and light-induced magnetic phases⁵ – via optical spectroscopy due to their high binding energy and large oscillator strength^{6–10}. The pronounced optical resonances due to excitons lie below the electronic gap and arise from the atomically thin, two-dimensional nature of quantum confinement and weak dielectric screening^{1,7,9–11}. In monolayer TMDCs, a valley degree of freedom^{12–14} emerges from the crystal structure with C₃ and broken inversion symmetries, which gives rise to lowest-energy excitonic states with 2-fold degeneracy that display opposite chiral selection rules. Beyond the lowest-energy optical excitations, excitons can also exist in hydrogenic internal states^{15–17}, known as Rydberg excitons, which by virtue of their relatively larger wavefunction^{7,18} offer a sensitive probe of exciton-electron, exciton-exciton, and other quasiparticle interactions – making them attractive candidates for optical quantum sensing^{19–21}. Additionally, Rydberg excitons offer a way to realize giant light-matter interaction (similar to Rydberg atoms) and can be studied in cavity quantum electrodynamics and nonlinear optical measurements^{22,23}. While typically observed in resonant reflection measurements^{11,24}, a number of recent studies on extremely high-quality TMDC samples have reported Rydberg excitons in photoluminescence (PL)^{16,25–28}. Although such states have been extensively characterized in MoS₂, MoSe₂, WS₂ and WSe₂,^{15,16,24–30} they have not been well explored in MoTe₂³⁰.

The 2H phase of monolayer MoTe₂ is semiconducting, with the smallest bandgap (in the near infrared) amongst the Mo-based TMDC materials^{31–38}. Several studies have reported a phase transition to the metallic-1T' phase, under high doping conditions, which may be useful in phase change photonics^{39,40}. The optical properties of MoTe₂ change dramatically under the extreme conditions of high doping, but even

at lower doping densities ($\sim 10^{11} \text{cm}^{-2}$), the excitonic properties are significantly altered and yield information about quasiparticle interactions – primarily exciton-electron dynamics^{26–28,41}. Because of the presence of heavy tellurium atoms, the spin–orbit coupling effects (~ 230 meV for valence band and ~ 43 meV for conduction band)⁴² and bright–dark A-exciton splitting (~ 25 meV)³⁵ in MoTe₂ are much more significant compared with the other Mo-based TMDCs. Additionally, MoTe₂ is one of the few van der Waals materials to emit near the silicon band-edge, and hence, an accurate understanding of the photophysics of the entire Rydberg series under different conditions of excitation density, temperature, and doping can guide future development of near-infrared optoelectronic and photovoltaic components, such as detectors, modulators, and light-emitting diodes.

In this work, we report results of experimental characterization of the optical properties of electrostatically gated monolayer MoTe₂, probed via photoluminescence measurements. Combining high-quality heterostructures and a resonant back-reflector geometry, we identify different optical transitions corresponding to the excitonic Rydberg series. The evolution of emission as a function of temperature, reveals a semiconductor-like behavior with quantitative estimation of zero-temperature energies and Rydberg exciton-phonon coupling strengths. By controlling the charge density in the monolayer MoTe₂ from charge neutrality to electron (hole) densities of $\sim 10^{12} \text{cm}^{-2}$, we find strong modulation of optical transitions and continuous tuning of the ground and excited state excitonic manifold – which is computed and illustrated in Figure 1a. We also perform first-principles calculations on the basis of many-body perturbation theory (MBPT) to obtain the excited-state properties of monolayer MoTe₂, including many-electron interactions. First-principles GW plus Bethe–Salpeter equation (GW-BSE) calculations with a new plasmon pole model developed⁴² to account for the dynamical screening of carriers show that the strong tunability is attributed to enhanced screening of the excitonic states from the increased electron density, as well as phase space filling, which leads to Pauli blocking of optical transitions. Our ab initio calculations also capture well the trion binding energy close to charge neutrality. Additionally, a linear line width broadening is observed, which is attributed to enhanced exciton-electron scattering with increasing carrier density and is in qualitative agreement with explicit calculations that consider the scattering of excitons to the degenerate Fermi sea.

Results

To efficiently probe the optical properties of monolayer MoTe₂ samples, we adopt a Salisbury-screen⁴³ geometry (electromagnetic simulation details are in the Supporting Information (SI) (B)), shown schematically in Figure 1b. The MoTe₂ is placed approximately a quarter wavelength away, from a back-reflector of optically thick gold, which also acts as the bottom electrode, to cause a destructive interference of the electromagnetic field at the monolayer, thereby enhancing light-matter interaction. This configuration results in a mild Purcell enhancement of the emission⁴⁴ ($F_p \sim 2$, where F_p is the Purcell factor; SI (C) allows efficient tuning of the Fermi level in MoTe₂ with the application of a gate voltage across the bottom hBN).

Measurements of the spatial dependence of PL at $T = 4$ K yield bright, uniform emission from the monolayer regions of the device. Figure 1c shows integrated PL counts, $I_{PL} = \int_{\lambda=800\text{nm}}^{1150\text{nm}} I(\lambda) d\lambda$, over a bandwidth from 800nm (~ 1.55 eV) to 1150nm (~ 1.07 eV). The bilayer regions exhibit lower emission and a broader peak, while very faint emission is seen from the multilayer regions. There have been reports investigating whether bilayer can become direct gap semiconductor at lower temperatures using emission spectroscopy because of the similar photoluminescence quantum yield³⁶, $PLQY = \gamma_r / (\gamma_r + \gamma_{nr})$, where γ_r, γ_{nr} are the radiative and non-radiative rates, respectively. From our measurements (shown in SI (D)), we find the ratio of the PLQY of the monolayer to bilayer to be three, indicating that the indirect to direct gap transition might happen when MoTe₂ is thinned to a bilayer. A representative PL spectrum (Figure 1d)

from one of the brightest monolayer spots shows sharp emission around 1.172 eV and 1.149 eV with linewidths of 7.13 and 8.77 meV, respectively, which we attribute to the A1s exciton and trion, as previously reported^{31,34–38}. Some of the cleanest regions of the sample show extremely narrow linewidths, narrowest obtained being ~4.48 meV, indicating high sample quality (shown in SI (E)).

Ab initio GW-BSE calculations using a modified plasmon pole model to account for dynamical screening associated with free carriers⁴² support our understanding of the experimental spectra and enable prediction of important optical properties, such as the quasiparticle band gap, optical resonance energies, and exciton binding energies. Within this formalism, one- and two-particle excitations can be calculated using state-of-the-art GW and GW-BSE approaches, respectively. Computational details are reported in SI (O–S) and elsewhere.⁴² In monolayer MoTe₂, the lowest interband excitonic transition is bright and occurs at the degenerate K and K' points in the Brillouin zone (Figure 1a). Because of spin-orbit coupling effects, a splitting of both the valence band maximum and conduction band minimum occurs, resulting into two distinct series of excitons, often labeled as A and B excitons. The optical gap computed with the first-principles GW-BSE approach, which also corresponds to the lowest-energy A1s exciton energy, is found at $E_{opt} = 1.09$ eV, in good agreement with the experimentally measured gap. The computed GW quasiparticle gap is $E_g = 1.58$ eV (see SI (Q) for details). Thus, we predict an exciton binding energy of $E_b = E_g - E_{opt} = 490$ meV for the lowest energy, optically bright excited state. Because of strong Coulomb interactions in low dimensions, charged excitons (trions) are expected to form in monolayer MoTe₂. We calculate the binding energy of the negatively charged exciton from first-principles by solving the corresponding equation of motion for three-quasiparticle-correlated bound states [see SI (S) for details] and obtain 20.6 meV [see SI (S)], which is in agreement with former reports³¹ and measured values of ~23 meV.

Additional luminescence peaks are seen at higher energies at 1.269 eV, 1.29 eV and 1.315 eV, and have been identified as the A2s trion, A2s exciton and A3s exciton, respectively, in accordance with previous reports on MoTe₂³⁰ and other TMDCs. The assignment of these excitonic and trionic peaks is in accordance with nomenclature that reflects how the exciton wave function transforms under the crystal symmetry in analogy with the hydrogen atom.⁴⁵ Our ab initio GW-BSE calculations [see SI (O,Q) for details] predict higher excited state excitons at 1.31, 1.35, and 1.43 eV, which correspond to the A2s, B1s, and A3s excitons, respectively. The slight discrepancy in the peak energies and reordering of the B1s and A3s exciton is likely related to the enhanced screening of MoTe₂ by the hBN dielectric, which is not considered in the calculations. The observation of Rydberg states up to 3s enables investigation of stronger Rydberg interactions, as well as photon-matter coupling, in MoTe₂. The line widths observed for these excited states are exceptionally narrow and are ~10 meV and ~25 meV for the 2s and 3s exciton, respectively. Additionally, the brightness of the 2s state is ~10% of the 1s state, which is comparable with or higher than that for other TMDCs.

To verify that the emission is excitonic in nature, we performed pump-power-dependent photoluminescence measurements. We scanned the incident pump fluence over two decades in intensity and observed an increase in the emission intensity (Figure 2a). A mild spectral broadening is associated with increasing pump density that originates from enhanced exciton–exciton interactions. We analyze the peaks by fitting them to a Lorentzian line shape profile,

$$I_{PL} = \sum_{i=Rydberg\ states} \frac{A_i \Gamma_i^2}{(\omega - \omega_i)^2 + \Gamma_i^2} \quad (I),$$

where A_i is the oscillator strength, Γ_i is the broadening and ω_i is the resonance frequency of each resonance, respectively. We can extract the integrated PL intensity, $\int I_{PL,i}(P) d\omega = C_{0,i} P^{\alpha_i}$, where P is the incident

power and α_i is the exponent for each resonance, $I_{PL,i}$ is given by eq 1 and $C_{0,i}$ is a dimensionless constant as a function of pump power. Near-linear scaling is seen for all the excitonic states as shown in Figure 2b with exponents as $\alpha = 1, 0.93$, and 0.92 for the 1s, 2s, and 3s states, respectively. This excludes any defect related emission as no saturation or non-linearity is observed over 2 orders of magnitude of incident pump power.

Rydberg excitons in MoTe₂ also show strong temperature dependence, which is consistent with previous observations in other TMDCs. While the lowest energy state has been investigated for MoTe₂, there is lack of knowledge about the excited state dynamics with temperature. Our measurements, in Figure 2 c,d, for the 1s and 2s exciton, respectively, show a redshift for excitonic states with increasing temperature, which can be modeled with a semiempirical semiconductor band gap dependence of the form

$$E_{exc}(T) = E_{exc}(0) - S < \hbar\omega > [\coth\left(\frac{<\hbar\omega>}{k_B T}\right) - 1], \quad (2)$$

where $E_{exc}(0)$ is the resonance energy at zero temperature limit, S is a dimensional constant, k_B is the Boltzmann constant and $< \hbar\omega >$ is the average phonon energy³⁴. From the fits, we extract the parameters summarized in Table T1, also shown in Figure 2 e,f. Furthermore, the PLQY drops with increasing temperature, which is attributed to an increase in accessible non-radiative decay channels from the phonon contributions (evident from the linewidth broadening with increasing temperature, shown in SI (I)), while the radiative contribution remains constant. The zero-limit exciton energy indicates the Rydberg state energy levels, which are in close agreement with ab initio GW-BSE computed energy levels (A1s = 1.09 eV and A2s = 1.31 eV), which correspond to $T = 0$ K. Interestingly, the relative intensity of the 2s exciton state with respect to the 1s state grows with increasing temperature [see SI (I)], which possibly stems from weaker coupling with the phonons.

Table 1. Experimentally Measured Zero-Temperature Exciton Energy and Exciton-Phonon Coupling Parameters for the Rydberg States

State index	Energy ($E_{exc}(0)$) (eV)	S	$<\hbar\omega>$ (meV)
1s	1.176 ± 0.019	1.22 ± 0.434	8.7 ± 7.009
2s	1.292 ± 0.018	1.08 ± 0.304	6.7 ± 5.825

Reduced dielectric screening and strong electron-hole Coulomb interactions in two-dimensional semiconductors make their electronic and optical properties highly sensitive to their dielectric environments^{9,11,17,41,46–48}. In particular, the presence of free carriers can significantly affect the electronic landscape of a TMD monolayer.^{26–29,31,41} A key finding of our study, summarized in Figure 3, is the carrier dependence of the exciton-electron interaction, as quantified by the gate-voltage dependence of the exciton and trion emission properties. We first focus near the 1s exciton resonance illustrated in Figure 3a-c. A false color map shows the evolution of the 1s exciton and trion peaks as a function of applied gate voltages ($V_g = -10$ to 10 V). At very low voltages, the neutral exciton peak dominates in emission, but with a very small change in the carrier density, the trion peak rapidly emerges as a dominant feature on either side of $V_g \approx -0.65$ V (which is identified as the charge neutral condition from the peak in neutral 1s exciton emission intensity). At higher voltages, the emission from the neutral exciton is completely suppressed. While trion emission grows in intensity for higher voltages, it eventually saturates and shows a slight reduction at even higher voltages. Such changes are better visualized in the derivative of PL with respect to energy (dPL/dE), as shown in Figure 3b,e for different regions of the gate voltage. The resonances corresponding to the 2s and 3s excitonic states show a qualitatively similar doping dependence (Figure 3d-f). Line cuts corresponding to near-charge neutral condition and finite doping showing strong exciton

and trion emission spectra are plotted in Figure 3 panel (c) for the 1s state and in panel (f) for the 2s and 3s states.

To quantitatively understand the doping-induced changes in the emission dynamics, the spectra are fitted to a sum of multiple Lorentzian features, as given by (eq 1), which correspond to the different exciton and trion states. The evolution of the peak intensity, line width, and energy are then extracted as a function of carrier density, with the results presented in Figure 4. Figure 4a,b quantifies the changes in the PL intensity of the different exciton and trion states, as discussed previously. A crossover density (N_c) is defined where the exciton and trion intensities overlap and is identified to be $V_g = 0.296$ V and $V_g = -1.36$ V on the electron and hole side, respectively, for the 1s state. This corresponds to [from a parallel plate capacitor model, see SI (G)] charge densities of $N_c^- = 2.08 \times 10^{11} \text{ cm}^{-2}$ and $N_c^+ = 1.54 \times 10^{11} \text{ cm}^{-2}$, respectively. Additionally, as seen in Figure 4e, the exciton slightly blue-shifts (2s much more than 1s) with increasing charge density, while the trion red-shifts [see SI (M)]. A qualitatively similar trend is seen for the features corresponding to the 2s exciton state and a crossover density of $V_g = 1.24$ V and $V_g = -2.42$ V, which corresponds to $N_c^- = 4.19 \times 10^{11} \text{ cm}^{-2}$ and $N_c^+ = 3.95 \times 10^{11} \text{ cm}^{-2}$ that are identified on the electron and hole side, respectively. The emission strength from the 3s trion state, which appears red-shifted to the 3s excitonic state, is not high enough to perform further quantitative analysis. However, from the derivative of PL measurements in Figure 3e,f, it is clear that a similar qualitative picture also holds true for the 3s state. Further studies with magnetic fields are required to study quantitative dynamics of the even higher states so that the visibility is improved. Our observations are consistent with previous reports of gate-tunable exciton and trion intensities in other TMDCs.^{26–28}

The energy differences ($\Delta E = E_{\text{exciton}} - E_{\text{trion}}$) between the exciton and trion exhibit an unusual gate dependence and show striking difference between the 1s and 2s states (Figure 4c). An overall slight blue shift of the energy difference $\Delta E_{1s} \sim 1 \text{ meV}$, over a doping density of $n \sim 1 \times 10^{12} \text{ cm}^{-2}$ is seen. A linear fit for ΔE_{1s} reveals a rate of change in the exciton energy $0.103 \text{ meV}/(10^{11} \text{ cm}^{-2})$ ($0.118 \text{ meV}/(10^{11} \text{ cm}^{-2})$) for the electron (hole) doping. A zero-density limit of the energy shift provides the trion binding energy which is 21.94 meV (22.14 meV) for the negative (positive) trion. The energy shift is highly exaggerated for the 2s state, where a much larger shift of $\Delta E_{2s} \sim 10 \text{ meV}$ is seen over a smaller doping density of $n \sim 5 \times 10^{11} \text{ cm}^{-2}$. A similar analysis yields $1.57 \text{ meV}/(10^{11} \text{ cm}^{-2})$ ($2.56 \frac{\text{meV}}{10^{11} \text{ cm}^{-2}}$) for the electron (hole) doped case. The trion binding energies are estimated to 18.14 meV (13.67 meV) for the negative (positive) side. The lower binding energy of the 2s trion compared with the 1s state follows from the lower binding energy of the corresponding neutral state. This unusually larger energy shift is understood as stemming from the larger wave function of the 2s state and, thus, higher susceptibility to the electronic landscape, which also is evident from the stronger dependence of the oscillator strength with doping density of the 2s state compared with the 1s state. These results are illustrated in Figure 4c and summarized in Table 2. In general, we expect the sensitivity of self-doping to increase dramatically with even higher-lying Rydberg states.

Table 2. Experimentally Measured Binding Energy and Energy Shifts for Rydberg Trions

State index	$E_{b,\text{trion}^+}(\text{meV})$	$E_{b,\text{trion}^-}(\text{meV})$	$\Delta E/\Delta n^+(\text{meV}/10^{11} \text{ cm}^{-2})$	$\Delta E/\Delta n^-(\text{meV}/10^{11} \text{ cm}^{-2})$
1s	22.14 ± 0.2	21.94 ± 0.1	0.118 ± 0.029	0.103 ± 0.023
2s	13.67 ± 0.12	18.14 ± 0.09	2.56 ± 0.16	1.57 ± 0.19

We also measure the linewidth evolution (Figure 4d) and observe that neutral exciton states exhibit linewidth broadening as a function of doping density. Additionally, while the 2s trion broadens, the 1s trion remains nearly unchanged with increasing carrier concentration.

Discussion

To better understand doping-induced changes in the optical properties, we use first-principles GW and GW-BSE calculations with a modified plasmon pole model⁴² to compute the exciton spectrum under different carrier densities. For optical excitations close to the band edge, we find two main effects to support our experimental observation: (i) a doping-independent ground exciton energy (Figure 5b) and (ii) a suppression of the exciton oscillator strength (Figure 5c). Numerical results are reported in Table 3.

Table 3. Computed Rydberg Exciton Binding Energy and Relative Dipole Moment as a Function of Doping Density

Doping density (cm^{-2})	A1s		A2s		A3s	
	ΔE_b (meV)	Rel. Osc.	ΔE_b (meV)	Rel. Osc.	ΔE_b (meV)	Rel. Osc.
0	0	1	0	0.25	0	0.09
2.3×10^{11}	-116	0.58	-64	0.08	-67	0.05
1.6×10^{12}	-246	0.28	-166	0.05	-164	0.02
3.0×10^{12}	-301	0.10	Not detectable			
4.5×10^{12}	-353	0.05				
5.9×10^{12}	-366	0.02				
8.7×10^{12}	-368	0.01				

The evolution of the exciton energy with increasing doping density arises from an interplay of various effects^{49–51}. In the low-doping regime, the doping-independent exciton energy results from a compensation between the band gap renormalization and exciton binding energy reduction (Figure 5a, b), which is expected from the reduced electron-hole Coulomb interaction. At a higher doping concentration, the ground exciton peak is expected to blue-shift slightly as the exciton binding energy saturates, while the quasiparticle gap slightly increases because of an increase of the energy continuum with the free carrier concentration.⁵⁰ In addition, as the doping density increases, the exciton delocalizes in real space [exciton wave function reported in SI (R)], and Pauli blocking prevents transitions around the K valley, which is eventually reflected in a decrease of the oscillator strength of the exciton peak, as shown in Figure 5c. This argument can be related to the intrinsically lower oscillator strength (and by reciprocity, lower PLQY) of the higher order Rydberg states, which is also due to a more delocalized wave function in real space. Similarly, the exciton binding energy and oscillator strength of the A2s and A3s excited states decrease rapidly, and the corresponding peaks quickly vanish above a doping density of $2 \times 10^{12} \text{ cm}^{-2}$.

The average lifetime, τ , of an unstable particle is related to the decay rate γ , as $\tau = 1/\gamma$. The PL linewidth L , obtained as $L = \hbar/\tau = \hbar\gamma$, provides information about intrinsic contributions from radiative exciton lifetime and dephasing from exciton-phonon scattering, as well as extrinsic inhomogeneous broadening effects (e.g., doping, defects, and substrate-induced disorder). In MoTe_2 monolayer, the bright exciton state is energetically below the dark states, which, at low temperature, prevents scattering toward intervalley exciton states that would require the absorption of a phonon. Therefore, at low temperature, the intrinsic contributions to the line width are dominated by radiative exciton decay.⁵² Using Fermi's golden rule,⁵³ we compute a radiative exciton lifetime of 0.3 ps, which corresponds to a radiative line width of 2.2 meV for the ground exciton. The discrepancy with the experimental zero-doping line width of 7.13 meV

comes from inhomogeneous broadening effects, such as the presence of defects or substrate effects. Furthermore, because of the presence of a back reflector, which gives rise to a slight Purcell enhancement in emission, it is expected that the enhanced radiative rate is higher than the computed one in vacuum (by approximately 2-fold). With increasing doping density, charged excited states, known as trions, emerge and couple to the excitons. Using the microscopic many-body theory developed in previous studies,⁵¹ we expect an approximately linear exciton line width broadening with doping density (~ 8.7 meV per 10^{12} cm⁻² doping density, in our measurements) because of enhanced exciton-electron scattering.

Conclusions

In summary, we report on the optical luminescence features of a monolayer MoTe₂, including Rydberg excitons up to 3s states, by combining results of experimental photoluminescence measurements and first principles calculations. We observe a linear dependence of the exciton peak energy with incident pump fluence and a red shift with increasing temperature that follows a semiempirical semiconductor relationship. The optical response can further be modulated with gate voltage due to an efficient exciton-to-trion conversion. With increasing doping density, we predict (i) a reduction in the exciton oscillator strength and (ii) a near-constant (mild blue shift) exciton energy, which supports our experimental measurements. Our understanding of MoTe₂ photophysics creates a foundation for the understanding and design of future optoelectronic devices in the near-infrared.

METHODS

Fabrication. SiO₂ (285 nm)/Si chips were cleaned with ultrasonication in acetone and isopropanol for 30 min each, followed by oxygen plasma treatment at 70 W and 300 mTorr for 5 min. Monolayer MoTe₂, few-layer hBN, and graphene flakes were directly exfoliated using Scotch tape at 100 °C to increase the yield of monolayer flakes. Monolayer thickness was initially identified using optical contrast ($\sim 7\%$ contrast per layer) and later verified with atomic force microscopy. hBN thickness was confirmed with atomic force microscopy. Flakes were assembled with a polycarbonate/polydimethylsiloxane (PC/PDMS) stamp with pick-up at temperatures between 80 - 110 °C. The entire heterostructure stack was dropped on prefabricated gates at 180 °C. The polymer was washed off in chloroform overnight, followed by isopropanol for 10 min. Given the air-sensitive nature of MoTe₂ monolayers, the exfoliation and identification of MoTe₂ flakes and the stacking of the entire heterostructures were done in a nitrogen-purged glovebox with oxygen and moisture levels below 0.5 ppm. Gates were fabricated on SiO₂ (285 nm)/Si chips with electron-beam lithography (PMMA 950 A4 was spun at 3500 rpm for 1 min and baked at 180 °C using a 10 nA beam current and dosage of 1350 μ C/cm² at 100 kV) and developed in methyl isobutyl ketone/isopropanol (1:3) for 1 min, followed by isopropanol for 30 s and electron beam evaporating with 5 nm Ti/95 nm Au at a 0.5 Å/s deposition rate. Liftoff was done in warm acetone (60 °C) for 10 min, followed by rinse in isopropanol for 5 min. The gates were precleaned before drop-down of heterostructure by annealing in high vacuum (2×10^{-7} Torr) at 300 °C for 6 h. The chip was then wire-bonded with aluminum wires onto a custom homemade printed circuit board.

Optical Spectroscopy. Low-temperature confocal photoluminescence measurements were performed in an attoDRY800 closed-cycle cryostat at base pressures of $<2 \times 10^{-5}$ mbar. The sample was mounted on a thermally conducting stage with Apiezon glue, and the stage was cooled using a closed-cycle circulating liquid helium loop. The temperature was varied between ~ 4 and 300 K. A 532 nm (Cobolt) continuous-wave laser was used as the excitation source, with power ranging between 10 nW and 1 mW and focused to a diffraction-limited spot. Emission was collected in a confocal fashion with a cryogenic-compatible apochromatic objective with an NA of 0.82 (for the visible and NIR range, LT APO VISIR) and dispersed onto a grating-based spectrometer (with 150 grooves per mm with a Silicon CCD; Princeton

Instruments HRS 300). Voltage was applied using a Keithley 2400. Data was acquired with home-written MATLAB codes.

Crystal Growth. MoTe₂ single crystals were grown by the chlorine-assisted chemical vapor transport (CVT) method. A vacuum-sealed quartz ampule with polycrystalline MoTe₂ powder and a small amount of TeCl₄ transport agent (4 mg per cm³ of ampules' volume) was placed in a furnace containing a temperature gradient so that the MoTe₂ charge was kept at 825 °C, and the temperature at the opposite end of the ampule was about 710 °C. The ampule was slowly cooled after 6 days of growth. The 2H phase of the obtained MoTe₂ flakes was confirmed by powder X-ray diffraction and transmission electron microscopy studies. Flakes obtained from the aforementioned source, as well as commercially available MoTe₂ (2D Semiconductors), were investigated with similar results.

AFM Imaging. Atomic force microscopy (AFM) was performed using Bruker Dimension Icon in tapping mode. Data analysis was performed in MATLAB.

ASSOCIATED CONTENT

Supporting Information

The Supporting Information is available free of charge at <https://pubs.acs.org/doi/10.1021/acsnano.3c00145>.

(A) Crystal growth, device fabrication, and experimental methods; (B) choice of optical geometry; (C) estimation of Purcell enhancement; (D) comparison of monolayer and bilayer PL spectra; (E) narrowest line width observed for A1s exciton; (F) optical image of MoTe₂ monolayers; (G) charge density calculation; (H) power-dependent emission spectrum; (I) temperature-dependent PL broadening and intensity; (J) gate-dependent PL fits; (K) gate dependence of additional spot; (L) absolute intensity of exciton and trion emission modulation; (M) energy shift of exciton and trion emission; (N) comparison of MoTe₂ with MoS₂, MoSe₂, WS₂, and WSe₂; (O) computational details; (P) computation of exciton dispersion; (Q) computed exciton absorption spectrum as a function of doping density; (R) computed exciton wave function for different doping densities; (S) computation of trion binding energy; (T) discussion on importance of MoTe₂ optical properties and its Rydberg series; (U) atomic force microscope image of MoTe₂ device; and (V) discussion on line width of excitons.

AUTHOR INFORMATION

Corresponding Author

Harry A. Atwater – Thomas J. Watson Laboratory of Applied Physics, California Institute of Technology, Pasadena, California 91125, United States; Kavli Nanoscience Institute, Pasadena, California 91125, United States; orcid.org/0000-0001-9435-0201; Email: haa@caltech.edu

Authors

Souvik Biswas – Thomas J. Watson Laboratory of Applied Physics, California Institute of Technology, Pasadena, California 91125, United States; Kavli Nanoscience Institute, Pasadena, California 91125, United States

Aur lie Champagne – Materials and Chemical Science Division, Lawrence Berkeley National Laboratory, Berkeley, California 94720, United States; Department of Physics, University of California Berkeley, Berkeley, California 94720, United States; orcid.org/0000-0002-6013-2887

Jonah B. Haber – Department of Physics, University of California Berkeley, Berkeley, California 94720, United States

Supavit Pokawanvit – Department of Applied Physics and Department of Materials Science and Engineering, Stanford University, Stanford, California 94305, United States

Joeson Wong – Thomas J. Watson Laboratory of Applied Physics, California Institute of Technology, Pasadena, California 91125, United States; Kavli Nanoscience Institute, Pasadena, California 91125, United States

Hamidreza Akbari – Thomas J. Watson Laboratory of Applied Physics, California Institute of Technology, Pasadena, California 91125, United States; orcid.org/0000-0002-6073-3885

Sergiy Krylyuk – Materials Science and Engineering Division, National Institute of Standards and Technology, Gaithersburg, Maryland 20899, United States

Kenji Watanabe – Research Center for Functional Materials, National Institute for Materials Science, Tsukuba 305-0044, Japan; orcid.org/0000-0003-3701-8119

Takashi Taniguchi – International Center for Materials, Nanoarchitectonics, National Institute for Materials Science, Tsukuba 305-0044, Japan; orcid.org/0000-0002-1467-3105

Albert V. Davydov – Materials Science and Engineering Division, National Institute of Standards and Technology, Gaithersburg, Maryland 20899, United States; orcid.org/0000-0003-4512-2311

Zakaria Y. Al Balushi – Thomas J. Watson Laboratory of Applied Physics, California Institute of Technology, Pasadena, California 91125, United States; orcid.org/0000-0003-0589-1618

Diana Y. Qiu – Department of Mechanical Engineering and Materials Science, Yale University, New Haven, Connecticut 06520, United States; orcid.org/0000-0003-3067-6987

Felipe H. da Jornada – Department of Materials Science and Engineering, Stanford University, Stanford, California 94305, United States; orcid.org/0000-0001-6712-7151

Jeffrey B. Neaton – Materials and Chemical Science Division, Lawrence Berkeley National Laboratory, Berkeley, California 94720, United States; Department of Physics, University of California Berkeley, Berkeley, California 94720, United States; Kavli Energy Nanosciences Institute at Berkeley, Berkeley, California 94720, United States

Complete contact information is available at:

<https://pubs.acs.org/10.1021/acsnano.3c00145>

Author Contributions

S.B. and H.A.A. conceived the project. S.B. fabricated MoTe₂-gated heterostructures and performed characterization, optical measurements, and analysis of the data. J.W., H.A., and Z.Y.A.B. assisted in optical measurements and discussions. A.C. led the MBPT calculations with help from J.B.H. and S.P. and inputs from F.H.J., D.Y.Q., and J.B.N. S.K. and A.V.D. provided MoTe₂ crystals, and K.W. and T.T. provided hBN crystals. S.B. wrote the manuscript with input from all authors. H.A.A. supervised the project.

Notes

The authors declare no competing financial interest.

Disclaimer: Certain commercial equipment, instruments, or materials are identified in this paper in order to specify the experimental procedure adequately. Such identification is not intended to imply recommendation or endorsement by the National Institute of Standards and Technology, nor is it intended to imply that the materials or equipment identified are necessarily the best available for the purpose.

This manuscript also appears on arXiv as Biswas, S.; Champagne, A.; Haber, J. B.; Pokawanvit, S.; Wong, J.; Akbari, H.; Krylyuk, S.; Watanabe, K.; Taniguchi, T.; Davydov, A. V.; Al Balushi, Z. Y.; Qiu, D. Y.; da Jornada, F. H.; Neaton, J. B.; Atwater, H. A. Rydberg Excitons and Trions in Monolayer MoTe₂. arXiv, February 7, 2023, 2302.03720. DOI: 10.48550/arXiv.2302.03720.

ACKNOWLEDGMENTS

The experimental measurements were obtained under support from the US Department of Energy Physical Behavior of Materials program, under grant DE-FG02-07ER46405. The electronic structure calculations for the development of the plasmon-pole model is supported by the US Department of Energy Center for Computational Study of Excited-state Phenomena in Energy Materials (C2SEPEM) - (Many-body perturbation theory calculations) and the Theory of Materials FWP (development of the plasmon-pole model) under contract No. DE-AC02-05CH11231. Computational resources are provided by the National Energy Research Scientific Computing Center (NERSC) and the Texas Advanced Computing Center (TACC) at The University of Texas at Austin, funded by the National Science Foundation (NSF) award 1818253, through allocation DMR21077. A.C. acknowledges the support from Wallonie Bruxelles International. A.V.D. and S.K. acknowledge support through the Material Genome Initiative funding allocated to the National Institute of Standards and Technology. K.W. and T.T. acknowledge support from the Elemental Strategy Initiative conducted by the Ministry of Education, Culture, Sports, Science and Technology (MEXT grant JPMXP0112101001); Japan Society for the Promotion of Science (JSPS KAKENHI grant JP20H00354); and Centers of Research Excellence in Science and Technology (CREST grant JPMJCR15F3), Japan Science and Technology Agency (JST). The authors thank Eoin Caffrey and Dr. Pin Chieh Wu for their support. D.Y.Q. acknowledges support by a 2021 Packard Fellowship for Science and Engineering from the David and Lucile Packard Foundation.

References:

1. Wang, G. *et al.* Colloquium: Excitons in atomically thin transition metal dichalcogenides. *Rev Mod Phys* **90**, 021001 (2018).
2. Xu, Y. *et al.* Correlated insulating states at fractional fillings of moiré superlattices. *Nature* **2020** 587:7833 **587**, 214–218 (2020).
3. Zhang, Z. *et al.* Correlated interlayer exciton insulator in heterostructures of monolayer WSe₂ and moiré WS₂/WSe₂. *Nature Physics* **2022** 18:10 **18**, 1214–1220 (2022).
4. Smoleński, T. *et al.* Signatures of Wigner crystal of electrons in a monolayer semiconductor. *Nature* **2021** 595:7865 **595**, 53–57 (2021).
5. Wang, X. *et al.* Light-induced ferromagnetism in moiré superlattices. *Nature* **2022** 604:7906 **604**, 468–473 (2022).

6. Zhu, B., Chen, X. & Cui, X. Exciton Binding Energy of Monolayer WS₂. *Scientific Reports* 2015 5:1 **5**, 1–5 (2015).
7. Qiu, D. Y., da Jornada, F. H. & Louie, S. G. Optical spectrum of MoS₂: Many-body effects and diversity of exciton states. *Phys Rev Lett* **111**, 216805 (2013).
8. Klots, A. R. *et al.* Probing excitonic states in suspended two-dimensional semiconductors by photocurrent spectroscopy. *Scientific Reports* 2014 4:1 **4**, 1–7 (2014).
9. Ugeda, M. M. *et al.* Giant bandgap renormalization and excitonic effects in a monolayer transition metal dichalcogenide semiconductor. *Nature Materials* 2014 13:12 **13**, 1091–1095 (2014).
10. Chernikov, A. *et al.* Exciton binding energy and nonhydrogenic Rydberg series in monolayer WS₂. *Phys Rev Lett* **113**, 076802 (2014).
11. Raja, A. *et al.* Coulomb engineering of the bandgap and excitons in two-dimensional materials. *Nature Communications* 2017 8:1 **8**, 1–7 (2017).
12. Xu, X., Yao, W., Xiao, D. & Heinz, T. F. Spin and pseudospins in layered transition metal dichalcogenides. *Nature Physics* 2014 10:5 **10**, 343–350 (2014).
13. Xiao, D., Liu, G. bin, Feng, W., Xu, X. & Yao, W. Coupled spin and valley physics in monolayers of MoS₂ and other group-VI dichalcogenides. *Phys Rev Lett* **108**, 196802 (2012).
14. Cao, T. *et al.* Valley-selective circular dichroism of monolayer molybdenum disulphide. *Nature Communications* 2012 3:1 **3**, 1–5 (2012).
15. Diware, M. S. *et al.* Dielectric function, critical points, and Rydberg exciton series of WSe₂ monolayer. *Journal of Physics: Condensed Matter* **30**, 235701 (2018).
16. Chen, S. Y. *et al.* Luminescent Emission of Excited Rydberg Excitons from Monolayer WSe₂. *Nano Lett* **19**, 2464–2471 (2019).
17. Chernikov, A. *et al.* Exciton binding energy and nonhydrogenic Rydberg series in monolayer WS₂. *Phys Rev Lett* **113**, 076802 (2014).
18. Qiu, D. Y., da Jornada, F. H. & Louie, S. G. Screening and many-body effects in two-dimensional crystals: Monolayer MoS₂. *Phys Rev B* **93**, 235435 (2016).
19. Popert, A. *et al.* Optical Sensing of Fractional Quantum Hall Effect in Graphene. *Nano Lett* **22**, 7363–7369 (2022).
20. Xu, Y. *et al.* Creation of moiré bands in a monolayer semiconductor by spatially periodic dielectric screening. *Nature Materials* 2021 20:5 **20**, 645–649 (2021).
21. Xu, Y. *et al.* Correlated insulating states at fractional fillings of moiré superlattices. *Nature* 2020 587:7833 **587**, 214–218 (2020).
22. Walther, V., Johne, R. & Pohl, T. Giant optical nonlinearities from Rydberg excitons in semiconductor microcavities. *Nature Communications* 2018 9:1 **9**, 1–6 (2018).

23. Gu, J. *et al.* Enhanced nonlinear interaction of polaritons via excitonic Rydberg states in monolayer WSe₂. *Nature Communications* 2021 12:1 **12**, 1–7 (2021).
24. Chernikov, A. *et al.* Exciton binding energy and nonhydrogenic Rydberg series in monolayer WS₂. *Phys Rev Lett* **113**, 076802 (2014).
25. Hill, H. M. *et al.* Observation of excitonic Rydberg states in monolayer MoS₂ and WS₂ by photoluminescence excitation spectroscopy. *Nano Lett* **15**, 2992–2997 (2015).
26. Wagner, K. *et al.* Autoionization and Dressing of Excited Excitons by Free Carriers in Monolayer WSe₂. *Phys. Rev. Lett.* **125**, 267401 (2020).
27. Goldstein, T. *et al.* Ground and excited state exciton polarons in monolayer MoSe. *J. Chem. Phys.* **153**, 071101 (2020).
28. Liu, E. *et al.* Exciton-polaron Rydberg states in monolayer MoSe₂ and WSe₂. *Nature Communications* 2021 12:1 **12**, 1–8 (2021).
29. Arora, A. *et al.* Excited-State Trions in Monolayer WS₂. *Phys Rev Lett* **123**, 167401 (2019).
30. Han, B. *et al.* Exciton States in Monolayer MoSe₂ and MoTe₂ Probed by Upconversion Spectroscopy. *Phys Rev X* **8**, 031073 (2018).
31. Yang, J. *et al.* Robust Excitons and Trions in Monolayer MoTe₂. *ACS Nano* **9**, 6603–6609 (2015).
32. Chen, B. *et al.* Environmental changes in MoTe₂ excitonic dynamics by defects-activated molecular interaction. *ACS Nano* **9**, 5326–5332 (2015).
33. Froehlicher, G., Lorchat, E. & Berciaud, S. Direct versus indirect band gap emission and exciton-exciton annihilation in atomically thin molybdenum ditelluride (MoTe₂). *Phys Rev B* **94**, 085429 (2016).
34. Helmrich, S. *et al.* Exciton–phonon coupling in mono- and bilayer MoTe₂. *2d Mater* **5**, 045007 (2018).
35. Ruppert, C., Aslan, O. B. & Heinz, T. F. Optical properties and band gap of single- and few-layer MoTe₂ crystals. *Nano Lett* **14**, 6231–6236 (2014).
36. Lezama, I. G. *et al.* Indirect-to-Direct Band Gap Crossover in Few-Layer MoTe₂. *Nano Lett* **15**, 2336–2342 (2015).
37. Arora, A. *et al.* Valley Zeeman splitting and valley polarization of neutral and charged excitons in monolayer MoTe₂ at high magnetic fields. *Nano Lett* **16**, 3624–3629 (2016).
38. Koirala, S., Mouri, S., Miyauchi, Y. & Matsuda, K. Homogeneous linewidth broadening and exciton dephasing mechanism in MoTe₂. *Phys Rev B* **93**, 075411 (2016).
39. Wang, Y. *et al.* Structural phase transition in monolayer MoTe₂ driven by electrostatic doping. *Nature* 2017 550:7677 **550**, 487–491 (2017).
40. Duerloo, K. A. N., Li, Y. & Reed, E. J. Structural phase transitions in two-dimensional Mo- and W-dichalcogenide monolayers. *Nature Communications* 2014 5:1 **5**, 1–9 (2014).

41. Sidler, M. *et al.* Fermi polaron-polaritons in charge-tunable atomically thin semiconductors. *Nat. Phys.* **13**, 255 (2017).
42. Champagne, A.; Haber, J. B.; Pokawanvit, S.; Qiu, D. Y.; Biswas, S.; Atwater, H. A.; da Jornada, F. H.; Neaton, J. B. Quasiparticle and Optical Properties of Carrier-Doped Monolayer MoTe₂ from First Principles. arXiv, March 21, 2023, 2303.12122. DOI: 10.48550/arXiv.2303.12122.
43. Fante, R. L. & McCormack, M. T. Reflection Properties of the Salisbury Screen. *IEEE Trans Antennas Propag* **36**, 1443–1454 (1988).
44. Lu, Y. J. *et al.* Dynamically controlled Purcell enhancement of visible spontaneous emission in a gated plasmonic heterostructure. *Nature Communications* **2017 8:1** **8**, 1–8 (2017).
45. Berghäuser, G. & Malic, E. Analytical approach to excitonic properties of MoS₂. *Phys Rev B Condens Matter Mater Phys* **89**, 125309 (2014).
46. Qiu, D. Y., da Jornada, F. H. & Louie, S. G. Environmental Screening Effects in 2D Materials: Renormalization of the Bandgap, Electronic Structure, and Optical Spectra of Few-Layer Black Phosphorus. *Nano Lett* **17**, 4706–4712 (2017).
47. Li, L. *et al.* Direct observation of the layer-dependent electronic structure in phosphorene. *Nature Nanotechnology* **2016 12:1** **12**, 21–25 (2016).
48. Bradley, A. J. *et al.* Probing the Role of Interlayer Coupling and Coulomb Interactions on Electronic Structure in Few-Layer MoSe₂ Nanostructures. *Nano Lett* **15**, 2594–2599 (2015).
49. Liang, Y. & Yang, L. Carrier plasmon induced nonlinear band gap renormalization in two-dimensional semiconductors. *Phys Rev Lett* **114**, 063001 (2015).
50. Gao, S., Liang, Y., Spataru, C. D. & Yang, L. Dynamical Excitonic Effects in Doped Two-Dimensional Semiconductors. *Nano Lett* **16**, 5568–5573 (2016).
51. Katsch, F. & Knorr, A. Excitonic theory of doping-dependent optical response in atomically thin semiconductors. *Phys Rev B* **105**, 045301 (2022).
52. Brem, S. *et al.* Intrinsic lifetime of higher excitonic states in tungsten diselenide monolayers. *Nanoscale* **11**, 12381–12387 (2019).
53. Palummo, M., Bernardi, M. & Grossman, J. C. Exciton radiative lifetimes in two-dimensional transition metal dichalcogenides. *Nano Lett* **15**, 2794–2800 (2015).

Figures:

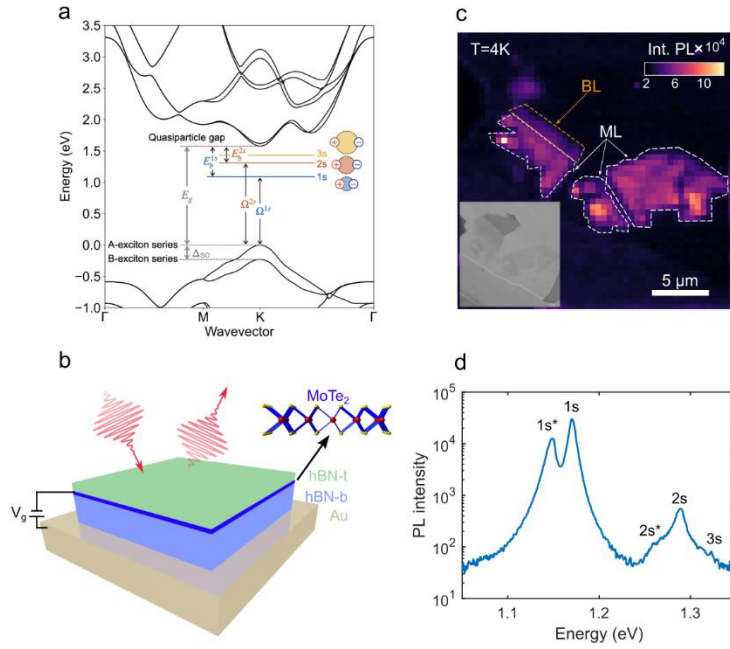


Figure 1. Electro-optic investigation of Rydberg excitons in monolayer MoTe₂. (a) Excitonic energy landscape of Rydberg series in monolayer MoTe₂ with the quasiparticle band structure, exciton-state energies Ω^S , and exciton binding energies E_b^S obtained using GW-BSE calculations. (b) Investigated device geometry consisting of hBN encapsulated monolayer MoTe₂ on Au substrate with applied gate voltage. (c) Integrated PL intensity map of investigated sample at 4K. Bright spots indicate monolayer. Inset is an optical micrograph of sample. (d) Example PL spectra with assigned Rydberg states.

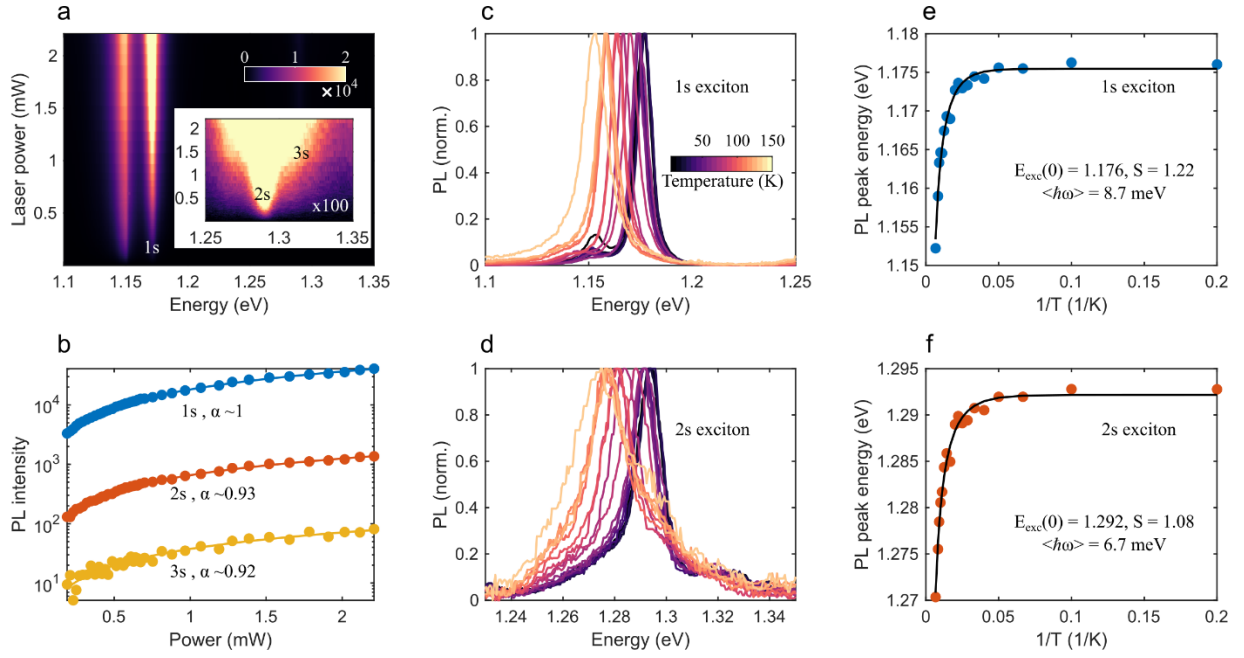


Figure 2. Pump power and temperature dependence of Rydberg excitons. (a) PL intensity variation with increasing pump power for the 1s exciton. Inset, PL ($\times 100$) for the 2s and 3s exciton. (b) Semilog-scale plot of intensity dependence of PL with pump power and corresponding fits to a power law showing excitonic emission ($I_{\text{PL}} = I_0 P^\alpha$). (c,d) Temperature variation of normalized PL spectrum for the 1s and 2s exciton regions, respectively. (e,f) Fits to a temperature model estimating different parameters for the 1s exciton and 2s exciton.

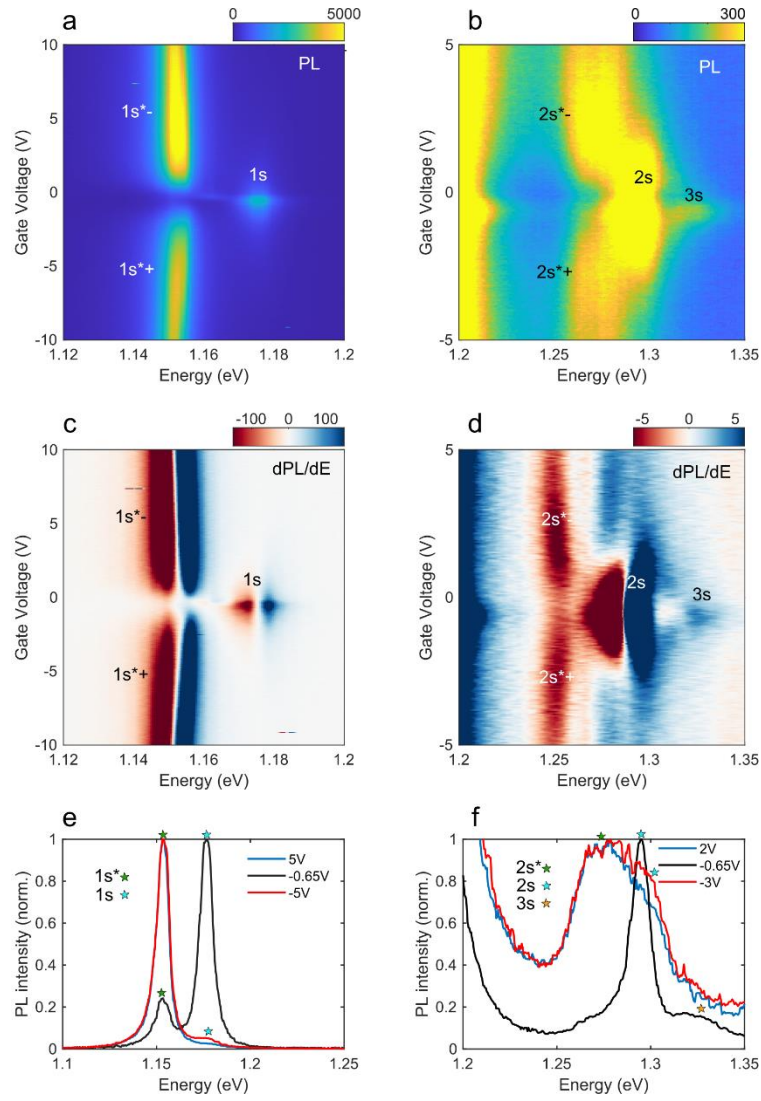


Figure 3. Gate-dependent PL spectra of Rydberg excitons. (a,d) PL intensity of different neutral exciton species and their corresponding trion features as a function of gate voltage near the 1s and 2s/3s resonances, respectively. (b,e) Derivative of the PL spectra, dPL/dE , shown in (a,d). (c,f) Line cuts of the PL spectrum at different voltages showing the different exciton and trion resonances.

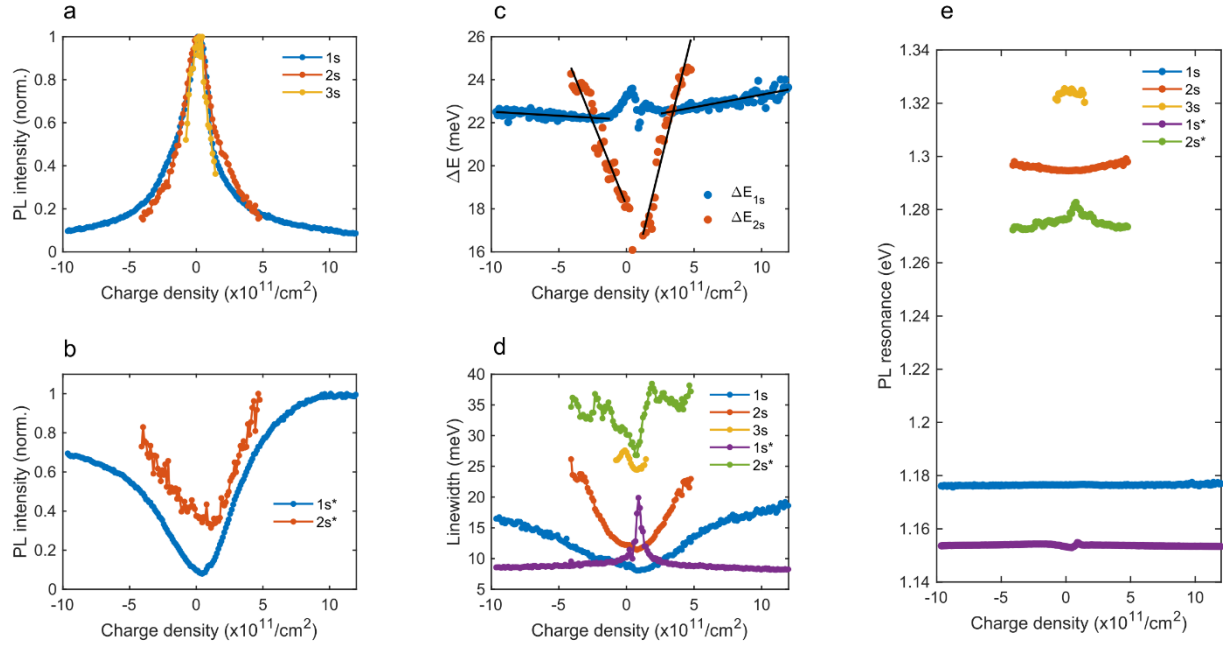


Figure 4. Gate-tunable PL properties of Rydberg excitons. (a,b) PL intensity (normalized) of different neutral exciton and trion species, respectively, as a function of charge density. (c) Energy shifts between the neutral exciton and the trion for 1s and 2s states as a function of charge density. (d) Evolution of the line width and (e) resonance energy of various exciton and trion states as a function of charge density.

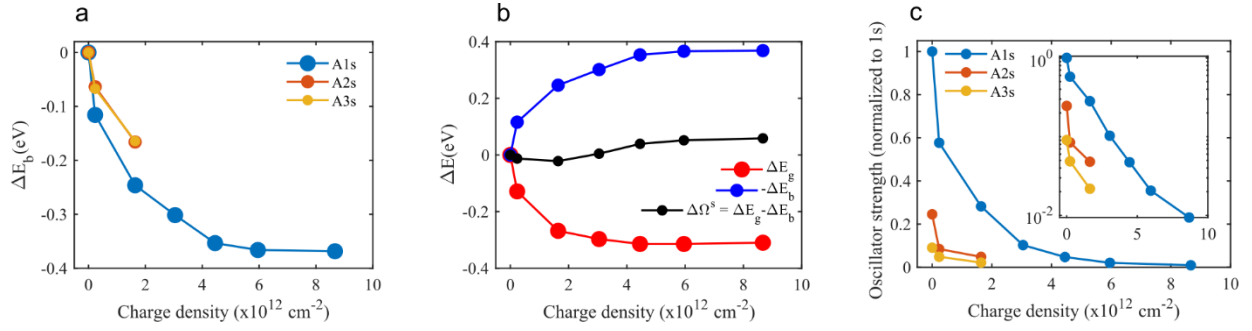


Figure 5. Doping dependence of (a) the variation in exciton binding energy, ΔE_b , for the ground A1s exciton, and the excited A2s and A3s states, (b) the variation in exciton energy $\Delta\Omega^s$ (black curve), the exciton binding energy ΔE_b (blue curve), and the renormalization of the QP band gap ΔE_g (red curve) for the ground A1s exciton, (c) the oscillator strength for the A1s, A2s and A3s states. Inset, same as (c) plotted in semilog-scale on the y axis.